Stormram 3: An MRI-compatible robotic system for breast biopsy

Vincent Groenhuis[1], Jeroen Veltman[2], Françoise J. Siepel[1] and Stefano Stramigioli[1]
[1]University of Twente, Enschede, The Netherlands
[2]Ziekenhuisgroep Twente, Almelo, The Netherlands
v.groenhuis@utwente.nl

***Abstract*—Stormram 3 is an MRI-compatible robotic system that can perform MR guided breast biopsies of suspicious lesions. The base of the robot measures 160x180x90 mm and it is actuated by five custom pneumatic linear stepper motors, driven by a valve manifold outside the Faraday cage of the MRI scanner. All parts can be rapidly prototyped with 3-D printing or laser-cutting, making the design suitable for other applications such as actuation in hazardous environments. Based on the choice of materials, the robot (with the exception of the needle) is inherently MR-safe. Measurements show that the maximum force of the T-49 actuator is 70 N, at a pressure of 0.3 MPa. The Stormram 3 has an optimized repeatability which is lower than 0.5 mm, and can achieve a positional accuracy in the order of 2 mm.**

I. Introduction

A. Clinical problem

Breast cancer is the most prevalent invasive cancer among women, accounting for about 25% of all cases worldwide. Early detection of malignant lesions is essential for successful treatment. Palpation can be used for self-examination, but its sensitivity is limited. To provide wider early detection of breast cancer, screening programs utilizing imaging techniques have been set up in many countries. For example, mammography can be used to produce detailed 2D x-ray images and is routinely used in periodic screening programs, with good sensitivity. Ultrasound (US) is also used to detect and analyze lesions in real-time.

MRI is an imaging technique with the highest sensitivity of lesion identification. Women with increased risk of breast cancer due to family history, and women with unspecific complaints may be offered MRI screening. MRI is also used to determine the optimal strategy for breast cancer surgery, as it can be used to determine whether a known cancer has metastatized to other parts of the breast.

When a suspicious lesion is found, a biopsy is needed for histopathological confirmation. The lesion is targeted with a biopsy needle, usually under ultrasound guidance, after which samples are collected. If the lesion is only visible on MRI and not on ultrasound, then the biopsy has to be performed under MRI guidance.

The current procedure of manual MRI-guided biopsy is a time consuming and costly procedure. The breast is first immobilized using fixation plates. After the initial scan and lesion localization, the patient is moved out of the scanner. The needle is then inserted blindly using a mechanical guide and a confirmation MRI scan is acquired. No imaging feedback is possible outside the scanner, which makes it difficult to compensate for unintentional tissue movements due to respiration and needle-tissue interactions. Therefore, needle placement inaccuracies must be compensated for by removing a large amount of tissue material causing additional discomfort. There is a need for improved systems for MRI-guided biopsy which are more precise and allow real-time imaging feedback, implying the need for an MRI-compatible robotic device.

Fig. 1: The MRI-compatible biopsy robot Stormram 3.

B. MRI-compatible actuators

The MRI scanner contains a strong magnetic field and utilizes radiofrequency signals. Ferromagnetic metals and electromagnetic signals inside the Faraday cage of the MRI scanner can distort the images, especially when placed near the scanning volume. Therefore, for optimal imaging quality the use of ferromagnetic and conductive materials and electronic devices have to be avoided or minimized.

One of the key challenges in creating an MRI-compatible device is actuation. As electromagnetic motors are ruled out, many alternatives have been explored: hydraulic [3], piezo [4], [5], cable transmission [6], MRI-driven [7], air turbine [8], flexible fluidic actuators [9], direct-acting pneumatic actuators [10], unidirectional pneumatic stepper motors [11], and especially bidirectional pneumatic stepper motors [1], [2],

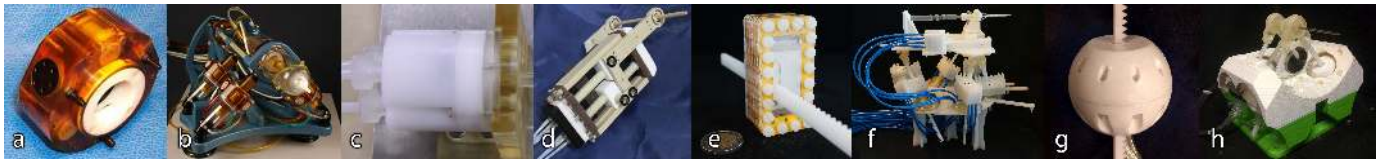

Fig. 2: State-of-the-art pneumatic stepper motors and robots: a. PneuStep rotational motor and b. McRobot by Stoianovici et al. [12]; c. Rotational motor and d. Two-DOF manipulator by Sajima et al. [13], [14]; e. Linear motor and f. Stormram 1 robot by Groenhuis and Stramigioli [1]; g. Linear motor and h. Stormram 2 by Groenhuis et al. [2].

[12]–[17]. Bidirectional pneumatic stepper motors have several important advantages: control is relatively straightforward by using a standard pneumatic valve manifold, a position feedback system is not necessary (provided that steps are never skipped), small leakages are acceptable because the medium is atmospheric air, and motors are scalable by changing cylinder cross-sectional areas.

C. MRI-compatible biopsy robots

A range of MRI-compatible biopsy robots have been developed. Su et al. developed multiple piezo/pneumatic-driven robots for prostate biopsy [18], in which the control electronics are placed in a shielded box inside the Faraday cage of the MRI scanner. Yang et al. [19] developed a piezo/pneumatic robotic system for breast biopsy. Stoianovici et al. developed the PneuStep (Figure 2a), a rotary stepper motor that is used for actuation of the MrBot (Figure 2b), designed for prostate biopsy interventions [12]. Sajima et al. also developed a rotary stepper motor (Figure 2c), for actuation of a two-DOF needle guiding manipulator (Figure 2d) [13], [14].

The authors of this paper developed a linear stepper motor (Figure 2e) for the Stormram 1 (Figure 2f), a 7 DOF needle manipulator based on the Stewart platform plus a needle insertion module [1]. The motor was minitiaturized in order to fit inside a 45 mm ball joint (Figure 2g), upon which the more compact, 5 DOF Stormram 2 robot was built (Figure 2h) [2].

The Stormram 2 demonstrated that it is possible to target lesions in a phantom breast with an accuracy of 6 millimetres [20]. Significant error sources arose due to clearances of the 3D printed ball joints, and in the coarse step size (1 mm) of the linear stepper motors. Furthermore, the workspace was limited and the motor forces insufficient to reliably operate the needle in dense tissue. The Stormram 3 robot was developed to address these shortcomings.

II. Design and implementation

Figure 1 shows the implementation of the Stormram 3, Figure 3a shows a 3D rendering and Figure 7 shows a kinematic diagram. Like its predecessor Stormram 2, it is a five-link parallel manipulator. It consists of one base (grey), three carriers (green), four blue stepper motors (blue with white racks), one T-49 stepper motor (grey with green rack) and a needle holder consisting of seven components (yellow/orange). The design and implementation of the different parts, motors and joints are described in this section.

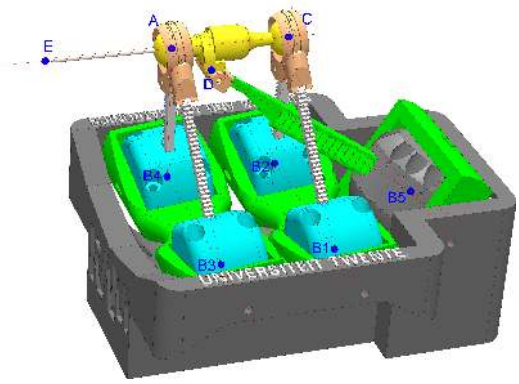

(a) Rendering with location of joint centroids A, $B1..B5$, C and D, and needle tip E.

Fig. 3: Stormram 3 kinematics.

A. Base and carriers

The base and carriers were printed with the Ultimaker 2 (Ultimaker BV, Geldermalsen, The Netherlands) in polyactic acid (PLA) material. Pin joints $J9, J6$ and $J12$ connect the front, middle and rear carriers to the base. Pin joints $J7, J8, J10, J11$ and $J13$ connect the five stepper motors to their carriers. All these joints are made of 4 mm acrylic rods, lubricated with petroleum jelly.

B. Stepper motors

For actuation of the five prismatic joints $J1..J5$, two different types of pneumatic linear stepper motors are used. Four copies of the blue motor, of which the centroids are located at positions $B_1..B_4$, actuate joints $J1-J4$. The actuated joint $J1$, for instance, controls the distance between points C and B_1. The more powerful T-49 motor with centroid at position B_5 actuates joint $J5$, driving the needle forwards and backwards.

1) Blue stepper motor: The blue stepper motor, shown in Figure 4a, is used to actuate four of the five degrees of freedom of the needle holder. The functional design is almost identical to that of the 45 mm spherical stepper motor (Figure 2g) used in the Stormram 2 robot [2]. The differences are that the step size is reduced from 1.0 mm to 0.67 mm for increased accuracy, and the motor's housing changed from a 45 mm sphere to a cylinder sized ⌀48 mm x 34 mm with holes for the pin joint. This eliminated the excessive clearance problem of the original 45 mm ball joints.

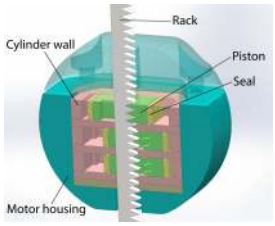

(a) Blue motor cutaway.

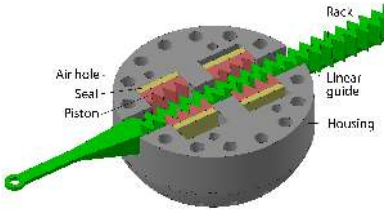

(b) T-49 motor cutaway view.

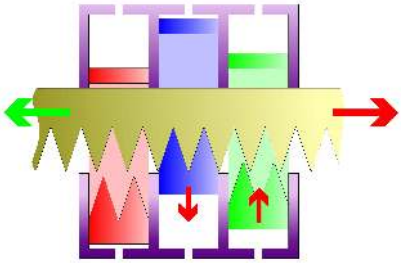

(c) Principle of operation of blue motor.

Fig. 4: Details of blue and T-49 stepper motors.

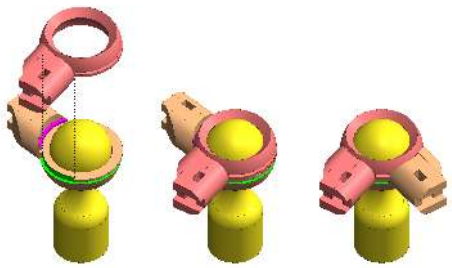

Fig. 5: The combined ball/revolute joint, in three stages of assembly. The red and orange parts are identical and both feature a rim (magenta) and groove (green). Left: the rim is aligned with an opening in the groove. Middle: parts matched, but not secured yet. Right: parts effectively interlocked, resulting in a combined ball/revolute joint.

The stepper motor's internal mechanism (Figure 4a) consists of laser-cut acetal parts, according to the design principles stated in Groenhuis and Stramigioli [1]. The cylinder case (pink) consists of seven plates that are stacked, forming three cavities in which toothed pistons (green) can slide, sealed by silicone seals (yellow). By pressurizing either chamber, the piston is pushed to the opposite side. The pistons themselves are laser-cut in a special way: after cutting out the top-view shape, the pistons are placed upright in a frame so that the teeth can be laser-cut from the side, resulting in a shape with the correct tooth geometry. The rack is also laser-cut from acetal; having a cross-section of $3.5 \times 4.0\,\mathrm{mm}$, these racks are somewhat flexible. This property has no influence on the rigidity of the needle holder, as forces are transferred in longitudinal direction only.

The bore's cross-sectional area A is $12 \times 5\,\mathrm{mm} = 60\,\mathrm{mm}^2$ and operating pressure $P = 0.3\,\mathrm{MPa}$, so the theoretical force F exerted by the pistons (ignoring friction losses) is $F = P \cdot A = 0.3 \cdot 10^6 \cdot 60 \cdot 10^{-6} = 18\,\mathrm{N}$. The three pistons interact with a rack of teeth with a pitch of 2 mm and a depth of 2.5 mm. The interaction is by means of a wedge mechanism: a piston displacement of 2.5 mm causes a rack displacement of 1.0 mm, so the wedge factor is $\alpha = \frac{2.5}{1.0} = 2.5$. Assuming ideal transfer of work (no energy dissipation or storage), the theoretical force exerted by the rack is calculated to be $2.5 \cdot 18 = 45\,\mathrm{N}$ (ignoring friction losses). The actual force has to be measured with a proper setup, and the difference between theoretical and actual force can be attributed to friction and pressure losses.

The principle of operation of the complete motor is shown in Figure 4c. When the green piston is pushed up and the blue one retracted, the rack moves one step to the right. This occurs because the three piston's jaws are phased 120° apart. By pressurizing the six chambers with appropiate waveforms, the position of the rack can be controlled in steps of 0.67 mm. When all three pistons are retracted, the rack can slide freely, which might be useful when considering medical robot safety in a clinical setting.

2) T-49 stepper motor: A new motor, the T-49 stepper motor, has been developed to drive the needle forwards and backwards. This motor measures $\varnothing 56 \times 40\mathrm{mm}$ and a CAD design is given in Figure 4b. It consists of six different custom parts: three housing parts, two identical pistons, four silicone seals and the rack. The silicone seals were hand-cut using a 3D printed mechanical guide, all other parts were 3D printed with the Ultimaker 2 in PLA material.

The novel part is that the T-49 has only two cylinders, in which pistons act on a double-sided rack. Also, the motor is fully 3D printed, eliminating the need of a separate housing required for the blue motor. In this way, the available space can be used more efficiently and the increased bore's cross-sectional area results in higher output forces. This cross-sectional area is $14 \times 14\,\mathrm{mm} = 196\,\mathrm{mm}^2$. Both teeth pitch and teeth depth are set to 4 mm. The step size is one quarter of the pitch, i.e. 1 mm. A piston displacement of 4 mm causes a rack displacement of 2 mm, so the wedge factor is $\alpha = \frac{4.0}{2.0} = 2.0$. When pressurized with a pressure of $P = 0.3\,\mathrm{MPa}$, the theoretical force exerted by the rack (ignoring friction losses) is $F_r = 2.0 \cdot 0.3 \cdot 10^6 \cdot 196 \cdot 10^{-6} = 118\,\mathrm{N}$, which is over 2.5 times the force of the blue motor. This makes inserting the needle in dense tissue and stiff lesions easier. Needle insertion forces in excess of 10 N may be needed in such cases.

The two pistons have a total of four jaws, phased 90° apart. One drawback is that it is not possible to arrange the pistons in a configuration that allows free sliding of the rack, although it is possible to move the rack manually by applying a certain force, when the chambers are all de-pressurized.

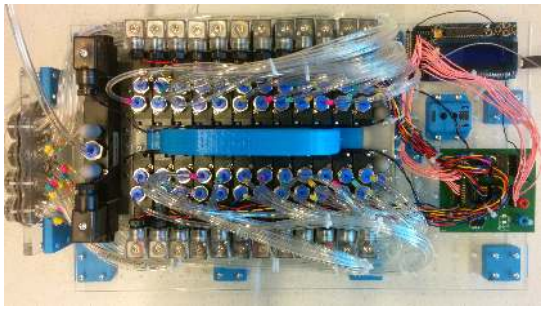

Fig. 6: Computer-controlled pneumatic distributor.

C. Needle holder

The needle holder consists of seven pieces that are printed with the Stratasys Objet Eden 250 (Stratasys Ltd, Eden Prairie, MN, USA) in FullCure720 material. The central shaft, connecting points A, C and D together, consists of two parts that are connected by a bayonet mount and accomodate a 12-gauge (2.1 mm) needle.

Joints $J16$ and $J17$ are combined ball/revolute joints, that consist of three parts, shown in Figure 5. The ball part (ball radius 9 mm) is enclosed by a pair of identical socket halves that are interlocked by a revolute joint inspired by the bayonet mount. Each of the two socket parts are rigidly attached to the racks of the stepper motors in the same carrier.

Finally, joints $J14$ and $J15$ are pin joints, together forming a universal joint which connects the rack of joint $J5$ to the needle holder. As for the base and carriers, $\varnothing 4$ mm acrylic rods connect the different parts together.

D. Pressure distributor

In order to drive the pneumatic stepper motors with appropiate waveforms, a pneumatic distributor was required. A manually-controlled distributor was developed for the Stormram 1 robot [1], and is also used to operate the Stormram 2 and 3 by visual servoing. As it is practically impossible to guide a biopsy needle in breast tissue by visual servoing alone, in the absence of realtime MRI, a computerized valve manifold (Figure 6) was also built. This manifold can control the different robots programmatically towards given target coordinates in feed-forward fashion. Both manifolds allow operation of the robot at a distance of 7 metres, as required because the controller cannot be placed inside the Faraday cage of the MRI scanner itself due to electromagnetic interference. Consequently, airflow limitations and transmission delays in the pneumatic lines restrict the motor's stepping frequency to approximately 5 Hz for the manual manifold [1], and 10 Hz for the computerized one.

III. Kinematics and workspace

In order to steer the needle along the desired trajectory towards a specific target, knowledge of the robot kinematics is required. In this section, the forward and inverse kinematics are described. The desired end-effector configurations can be translated to actuator configurations, and vice versa.

A. Coordinate system

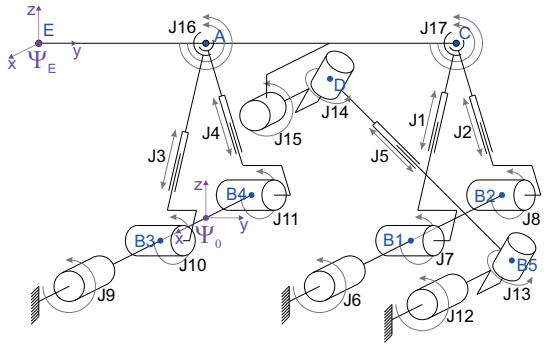

Fig. 7: Kinematic diagram of Stormram 3, with coordinate systems Ψ_0 and Ψ_E.

Figure 7 shows the kinematic diagram of Stormram 3 and defines two coordinate frames. Frame Ψ_0 is attached to the base of the robot, and Ψ_E is attached to the needle holder. The coordinate transformation from Ψ_0 to Ψ_E is represented as H_0^E. The Stormram 3 pose is fully defined by this transformation, as all joint centroids are rigidly attached to either Ψ_0 or Ψ_E.

The actuated joint configuration vector $\mathbf{v} = (\ell_1, \ell_2, \ell_3, \ell_4, \ell_5)$ defines the state of the five prismatic actuators. A length ℓ_i represents the distance between the joint centroids that are linked by the i-th prismatic joint.

The forward kinematics problem can now be defined as finding H_0^E from a given $\mathbf{v}$. The inverse kinematics problem involves finding $\mathbf{v}$ for a given H_0^E with one free parameter, because only five degrees of freedom can be controlled.

B. Forward kinematics

As the Stomram 3 is a parallel manipulator, derivation of H_0^E from a given $\mathbf{v}$ is not trivial. A 3D coordinate transformation has six degrees of freedom. Therefore, six constraints are needed to define H_0^E.

The first step is to constrain the points A and C to one degree of freedom. We can observe that the triangle ΔAB_3B_4 defines a plane, intersecting the XY plane in Ψ_0 along the $B3$-$B4$ line. As for a given $\mathbf{v}$, all sides of this triangle are determined, point A must lie on a circle around the $B3$-$B4$ axis with known midpoint and radius (given by the lengths of the ΔAB_3B_4 triangle). Likewise, point C must lie on another circle around the $B1$-$B2$ axis, with origin and radius given by the lengths of the ΔCB_1B_2 triangle.

The second step is to fix the distance between points A and C as defined by the needle holder geometry, constraining the number of DOFs of Ψ_E to two because the orientation of Ψ_E around its Y-axis is still free.

The third step is to apply the constraint put by the serial kinematic chain $J12 - J13 - J5 - J14 - J15$. This chain has four free parameters (as $J5$ is fixed), thus fixing $(6 - 4) = 2$ degrees of freedom of Ψ_E, making the Stormram 3 a well-determined kinematic system. Unfortunately, there is no elegant way to express this last constraint mathematically

without having to write out the full kinematic chain with all its joints.

To get a practically workable system for forward kinematics, it is proposed to start with an approximation, combined with an estimation of the error. The approximation is based on the observations that AD and DB_5 are approximately collinear and D is relatively close to A. Thus, one can approximate AB_5 as follows:

$$||AB_5|| \approx ||B_5D|| + ||AD||$$

With an approximation of the error ε:

$$\varepsilon \approx ||AD||(1 - \cos \angle B_5AD)$$

All coordinates can now be calculated with basic goniometry methods. It is possible to reduce the error by iteratively repositioning A based on the actual distance AB_5, but if the exact solution is needed then a more computationally intensive approach is required.

C. Inverse kinematics

The inverse kinematics problem states finding the joint vector $\mathbf{v} = (\ell_1, \ell_2, \ell_3, \ell_4, \ell_5)$ for a given end-effector configuration H_0^E with one free parameter, chosen to be the rotation around the Y-axis in the Ψ_E coordinate frame because the needle is axially symmetric.

Derivation of the coordinates of points A and C is trivial, and the lengths $\ell_1..\ell_4$ can be calculated directly. The fifth length, ℓ_5, can be approximated or numerically solved analogous to the forward kinematics problem problem.

Stepper motors are discrete, so in general $\mathbf{v}$ is not in the joint configuration space V. The blue stepper motor has a 0.67 mm step size, and for the T-49 motor it is 1.0 mm. Ignoring constant offsets, we have $\mathbf{v'} = (\frac{2}{3}n_1, \frac{2}{3}n_2, \frac{2}{3}n_3, \frac{2}{3}n_4, n_5)$ with $n_i \in \mathbb{N}$. A simplistic solution is to use the nearest values for $\mathbf{v}_i$ in V, but this might result in a significant error in the end-effector position. A better approach takes into consideration that needle tip positional accuracy takes precedence over angle accuracy, so when a range of insertion angles is possible, the one which minimizes the end-effector position error can be chosen.

D. Workspace calculation

Figure 8 shows a visualization of the reachable workspace of the needle tip, taking the most important physical constraints into account. The voxel size is $2.0 \times 2.0 \times 2.0\,\mathrm{mm}$ and the workspace is the union of all voxels that the needle tip can reach. The volume was found to be 2.0 L, but due to unmodeled physical constraints, the actual volume is slightly smaller.

IV. Measurements

Several measurements were performed to assess the performance of the joints, the two motor types and the repeatability of the Stormram 3 robot.

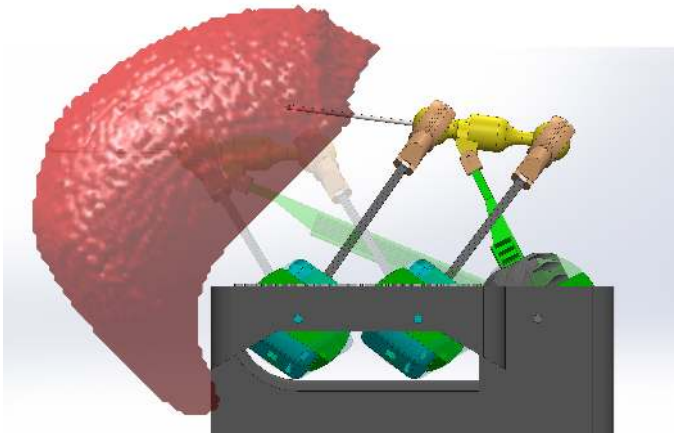

Fig. 8: Visualization of the workspace (red), with the Stormram 3 shown in two extreme configurations.

Extensive quantitative accuracy measurements on breast phantoms inside a MRI scanner were performed with the Stormram 2 robot controlled by the computerized manifold. These experiments are described in Abdelaziz et al. [20]. Based on an analysis of these experiments and repeatability measurements of the Stormram 3, the positional accuracy of Stormram 3 is estimated.

A. Friction and clearances in joints

The pin joints in the base and carriers, joint $J6 - J13$, were found to have no measurable backlash. There is no clearance around the pins, and the structure of the base, carriers and motors are sufficiently rigid to limit parasitic movements below 0.1 mm. The static friction in the joints were measured to be up to 0.02 N m.

The combined ball/revolute joints in the needle holder have a certain clearance. When the joints are dry, this results in parasitic movements in the order of 0.2 mm. After lubrication with petroleum jelly the parasitic movements are reduced to below 0.1 mm during normal operation.

B. Repeatability measurements

The repeatability of the Stormram 3 was evaluated using the manual valve manifold and a sheet of paper rigidly attached to a fixed object. By sequentially adjusting rack lengths $\ell_1..\ell_5$ by a known number of steps, the needle pierced holes with diameter 0.5-1.0 mm at five different locations on the sheet. By repeatedly moving the needle to the same joint configurations (taking care of hysteresis in the joints by keeping the approach consistent), it was observed that the needle always enters a hole that was already formed in this particular joint configuration. The result is that the Stormram 3 has a repeatability of better than 0.5 mm.

C. Stepper motor measurements

The blue and T-49 stepper motors were characterized by measuring its maximum pulling force as a function of the

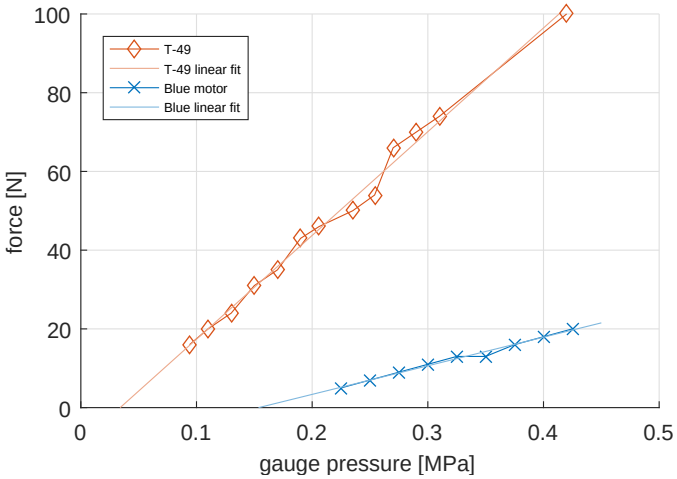

Fig. 9: T-49 and blue motor force versus pressure.

gauge pressure. Figure 9 shows their pressure-force relationship. At a pressure of 0.3 MPa, which is the standard working pressure of Stormram 3, the blue motor exerts 16 N of force while the T-49 can exert 70 N of force. The calculated theoretical values were 45 N and 118 N, respectively. The resulting mechanical efficiency is 36% for the blue motor, and 59% for the T-49 motor.

D. MRI tests

Qualitative MRI tests were performed with the Esaote G-scan Brio 0.25 T scanner. A phantom breast made of PVC with plasticizer, filled with fish oil capsules, was immobilized in a frame and placed in the MRI scanner. The Stormram 3 robot was positioned adjacent to the frame, and operated using visual servoing to insert the needle and examine any artifacts. See Figure 10a for the test setup, Figure 10b for one MRI slice and Figure 10c for a 3D rendering showing the phantom and a few markers.

The Stormram 3 robot (without needle) was found to have no measurable influence on MRI scans. After equipping it with a MRI-compatible, 14-gauge (2.1 mm) titanium needle and inserting it in a phantom, a susceptibility artifact up to a distance of 4 mm around the needle was observed.

Extensive quantitative measurements were performed with the Stormram 2 robot, controlled by the computerized manifold. These measurements are described in Abdelaziz et al. [20] and the average targeting error was found to be 6 mm.

V. Discussion

The Stormram 3 robot is a significant improvement over its predecessor. The T-49 motor can exert 70 N of force, making it suitable for targeting lesions in dense tissue. Due to the different kinematic design, the workspace has been increased and parasitic movements in the joints in the base have been effectively eliminated.

In ex-vivo MRI tests, the Stormram 2 has shown to have a targeting accuracy of 6 mm on average [20]. This error can be attributed to parasitic movements in joints, geometry

(a) Stormram 3 in the 0.25T MRI scanner.

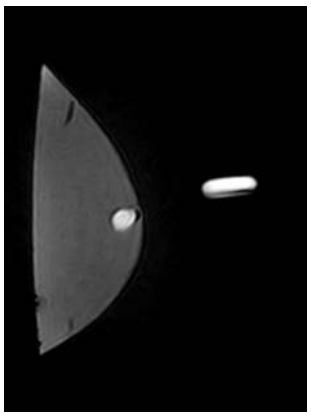

(b) One MRI slice, visualizing markers in the breast phantom and attached to the (invisible) needle.

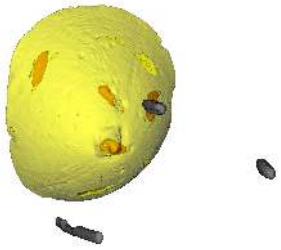

(c) Rendering of phantom (yellow) with embedded markers (orange), and markers attached to the Stormram 3 base (grey), rendered by 3D Slicer software.

Fig. 10: MRI test setup and scanning results.

approximations in the kinematics, discretization of the racks, hysteresis in linear stepper motors, offsets in calibration, needle deflection due to needle-tissue interaction and needle position measurement inaccuracies. Of these errors, the parasitic movements in joints have been effectively eliminated in the Stormram 3, and discretization errors have been reduced due to the smaller step size of 0.67 mm. Inaccuracies in kinematic calculations, calibration and hysteresis can be solved by a more sophisticated software implementation that precisely models the kinematics and actuator characteristics of the robot. In this way, and taking into account the repeatability of better than 0.5 mm, it is expected that the Stormram 3 can have a needle-tip positioning accuracy of as small as 2 mm.

The Stormram 3 robot (without needle) is entirely made from materials (plastics, silicone, nylon, photopolymer) that are considered to be safe with regard to the MR environment, and therefore does not distort the resulting MR images.

The kinematic design of the Stormram 3, with the five-link parallel actuator, is similar to that of the MrBot (Figure 2b). One important difference is that the MrBot has one extra degree of freedom to translate the needle holder longitudi-

nally. This is essential in obtaining smooth, linear needle trajectories in biological tissue, and to obtain a sufficiently large workspace. While it is possible to develop this for the Stormram 3 as well, it also makes the needle less accessible, complicating the biopsy procedure.

Several additional steps are required to advance the Stormram 3 further towards a complete market product that can potentially replace the current manually-operated MRI-guided breast biopsy procedure. A biopsy needle firing mechanism should be embedded, which can be triggered by the radiologist without the need to open the robot to swap needles. A comfortable patient bed with good fixation mechanism is essential. Software that combines pre-operative MRI scans with a needle path trajectory planning system and post-insertion validation needs to be developed. This software should also be able to take care of breast deformations, which could be performed in several ways. By using an elastographic model of the breast, deformations could be simulated and be accounted for. An alternative approach would be to acquire one or more intermediate scans during insertion of the needle, allowing to adjust the path based on these near-realtime scans.

VI. Conclusion

The Stormram 3 has shown that pneumatic linear stepper motors are an effective way of actuating MRI-compatible robots. Excluding the off-the-shelf needle, the robot is inherently MRI-compatible by the choice of materials. It can be driven by either a manually-operated pneumatic distributor using visual servoing, or programmatically using a computer-controlled valve manifold. The robot has shown to have sufficiently high stiffness and negligible parasitic movements. The needle tip repeatability is better than 0.5 mm, and based on the evaluation of the accuracy of Stormram 2, it is expected that in MRI experiments with the Stormram 3 using more sophisticated software, the needle tip positioning error can be kept in the order of 2 mm.

The technology developed in Stormram 3 is not limited to applications in MRI-compatible breast biopsy robots. Biopsies in prostate and other surgical interventions under MRI guidance may also benefit from a compact MRI-compatible robot driven by pneumatic linear stepper motors. As the powerful T-49 pneumatic stepper motor is relatively easy to produce and assemble, it may also find its way to applications outside the MRI scanner whenever pressurized air supply is available.

References

[1] V. Groenhuis and S. Stramigioli, "Laser-Cutting Pneumatics," in IEEE/ASME Transactions on Mechatronics, vol. 21, no. 3, pp. 1604-1611, June 2016. doi: 10.1109/TMECH.2015.2508100

[2] V. Groenhuis, J. Veltman and S. Stramigioli, "Stormram 2: A MRI-compatible pneumatic robotic system for breast biopsy," Proceedings of The Hamlyn Symposium on Medical Robotics, June 2016, Imperial College and the Royal Geographical Society, London, UK, pp. 52-53.

[3] Whitney, J. P., Glisson, M. F., Brockmeyer, E. L., and Hodgins, J. K., "A low-friction passive fluid transmission and fluid-tendon soft actuator." In 2014 IEEE/RSJ International Conference on Intelligent Robots and Systems (pp. 2801-2808).

[4] Su, H., Zervas, M., Cole, G. A., Furlong, C., and Fischer, G. S, "Real-time MRI-guided needle placement robot with integrated fiber optic force sensing." In Robotics and Automation (ICRA), 2011 IEEE International Conference on (pp. 1583-1588). IEEE.

[5] P. Moreira, S. Misra, "MR-Compatible Robot for Needle-Based Prostate Interventions." Proceedings of The Hamlyn Symposium on Medical Robotics 25-28 June 2016, Imperial College London and the Royal Geographical Society, London, UK

[6] Chapuis, D., Gassert, R., Ganesh, G., Burdet, E. A. B. E., and Bleuler, H. A. B. H., "Investigation of a cable transmission for the actuation of MR compatible haptic interfaces." In The First IEEE/RAS-EMBS International Conference on Biomedical Robotics and Biomechatronics, 2006. BioRob 2006. (pp. 426-431).

[7] Felfoul, O., Becker, A., Bergeles, C., and Dupont, P. E, "Achieving commutation control of an MRI-powered robot actuator." IEEE Transactions on Robotics, 31(2), 387-399 (2015).

[8] Elhawary, H., Zivanovic, A., Tse, Z. T. H., Rea, M., Davies, B. L., Young, I, Bydder, G., Payley, M. and Lamperth, M. U., "A magnetic-resonance-compatible limb-positioning device to facilitate magic angle experiments in vivo." Proceedings of the Institution of Mechanical Engineers, Part H: Journal of Engineering in Medicine, 222(5), 751-760.

[9] Comber, D. B., Slightam, J. E., Barth, E. J., Gervasi, V. R., and Webster, R. J., "Design and precision control of an MR-compatible flexible fluidic actuator." In ASME/BATH 2013 Symposium on Fluid Power and Motion Control. American Society of Mechanical Engineers, 2013

[10] B. Yang, U. X. Tan, A. B. McMillan, R. Gullapalli, and J. P. Desai, "Design and control of a 1-DOF MRI-compatible pneumatically actuated robot with long transmission lines," IEEE/ASME Trans. Mechatronics, vol. 16, no. 6, pp. 10401048, 2011.

[11] Y. Chen, C. D. Mershon, Z. Tsz, and H. Tse, "A 10-mm MR-Conditional Unidirectional Pneumatic Stepper Motor," IEEE/ASME Transactions on Mechatronics, Vol. 20, no. 2, April 2015, pp. 782788.

[12] Stoianovici, D., Patriciu, A., Petrisor, D., Mazilu, D., and Kavoussi, L., "A new type of motor: pneumatic step motor." IEEE/ASME Transactions On Mechatronics, 12(1), 98-106, 2007.

[13] H. Sajima, I. Sato, H. Yamashita, T. Dohi, and K. Masamune, "Two-DOF non-metal manipulator with pneumatic stepping actuators for needle puncturing inside open-type MRI," World Autom. Congr. (WAC), 2010, no. 1, pp. 38, 2010.

[14] Sajima, H., Kamiuchi, H., Kuwana, K., Dohi, T., and Masamune, K., "MR-safe pneumatic rotation stepping actuator." Journal of Robotics and Mechatronics, Vol. 24, No. 5, 2012, pp. 820-827, 2012.

[15] Y. Chen, K. W. Kwok, and Z. T. H. Tse, "An MR-Conditional High-Torque Pneumatic Stepper Motor for MRI-Guided and Robot-Assisted Intervention," Ann. Biomed. Eng., vol. 42, no. 9, pp. 18231833, 2014.

[16] Secoli, R., Robinson, M., Brugnoli, M., and y Baena, F. R., "A low-cost, high-field-strength magnetic resonance imagingcompatible actuator." Proceedings of the Institution of Mechanical Engineers, Part H: Journal of Engineering in Medicine, 229(3), pp. 215-224, 2015.

[17] Z. Guo, T. T. L. Lun, Y. Chen, H. Su, D. T. M. Chan, K.W. Kwok, "Novel Design of an MR-safe Pneumatic Stepper Motor for MRI-guided Robotic Interventions," Proceedings of The Hamlyn Symposium on Medical Robotics 25-28 June 2016, Imperial College London and the Royal Geographical Society, London, UK, pp. 50-51.

[18] H. Su, G. a. Cole, and G. S. Fischer, "High-Field MRI-Compatible Needle Placement Robots for Prostate Interventions: Pneumatic and Piezoelectric Approaches," Intell. Syst. Ref. Libr., vol. 26, pp. 332, 2012.

[19] B. Yang, S. Roys, U.-X. Tan, M. Philip, H. Richard, R. P. Gullapalli, and J. P. Desai, "Design, development, and evaluation of a master-slave surgical system for breast biopsy under continuous MRI," Int. J. Rob. Res., vol. 33, pp. 616630, 2013.

[20] M.E.M.K. Abdelaziz, V. Groenhuis, J. Veltman, F.J. Siepel and S. Stramigioli, "Controlling the Stormram 2: An MRI-compatible Robotic System for Breast Biopsy". 2017 IEEE International Conference on Robotics and Automation (ICRA), Singapore, 2017, pp. In press.